

# Correlation between structural, ferroelectric, piezoelectric and dielectric properties of $\text{Ba}_{0.7}\text{Ca}_{0.3}\text{TiO}_3\text{-}x\text{BaTi}_{0.8}\text{Zr}_{0.2}\text{O}_3$ ( $x = 0.45, 0.55$ ) ceramics

Bhavna C. Keswani<sup>a</sup>, S.I. Patil<sup>a</sup>, A.R. James<sup>b</sup>, Y.D. Kolekar<sup>a,\*</sup>, C.V. Ramana<sup>c,\*</sup>

<sup>a</sup> Department of Physics, Savitribai Phule Pune University, Pune 411007, Maharashtra, India

<sup>b</sup> Defence Metallurgical Research Laboratory, Hyderabad 500058, India

<sup>c</sup> Department of Mechanical Engineering, University of Texas at El Paso, El Paso, TX 79968, USA



## ARTICLE INFO

### Keywords:

Lead-free ferroelectrics  
Morphotropic phase boundary region  
Ferroelectrics  
Piezoelectric coefficients

## ABSTRACT

We report on the correlation between structural, ferroelectric, piezoelectric and dielectric properties of the  $(1-x)\text{Ba}_{0.7}\text{Ca}_{0.3}\text{TiO}_3\text{-}x\text{BaTi}_{0.8}\text{Zr}_{0.2}\text{O}_3$  ( $x = 0.45, 0.55$ ; abbreviated as 55BCT30 and 45BCT30) ceramics close to morphotropic phase boundary (MPB) region. The 55BCT30 and 45BCT30 ceramics were synthesized by the standard, high-temperature solid state ceramic method. X-ray diffraction (XRD) along with Rietveld refinement indicate that the 55BCT30 ceramics exhibit rhombohedral (*R*, space group *R3m*), orthorhombic (*O*, space group *Amm2*) and tetragonal (*T*, space group *P4mm*) phases while 45BCT30 ceramics exhibit only *T* and *O* phases. The temperature dependent Raman spectroscopy measurements confirm the structure and phase transformations observed from XRD. All the ceramics are chemically homogeneous and exhibit a dense microstructure with a grain size of 5–7  $\mu\text{m}$ . The presence of polarization-electric field and strain-electric field hysteresis loops confirm the ferroelectric and piezoelectric nature of the ceramics. The polarization current density-electric field curves show the presence of two sharp peaks in opposite directions indicating the presence of two stable states with opposite polarity. Higher values of direct piezoelectric coefficient ( $d_{33} \sim 360$  pC/N) were observed due to the existence of low energy barrier near MPB region and polymorphism. The 55BCT30 ceramics exhibit a higher value of electrostrictive coefficient ( $Q_{33} \sim 0.1339$  m<sup>4</sup>/C<sup>2</sup>) compared to the well-known lead-based materials. The temperature dependent dielectric measurements indicate the *O* to *T* phase transition for 55BCT30 and 45BCT30. These ceramics exhibit a Curie temperature ( $T_c$ ) of 380 K with a dielectric maximum of  $\sim 4500$ .

## 1. Introduction

Piezoelectric materials, which convert mechanical energy into electrical energy and vice versa, are widely used in a variety of applications such as piezoelectric sensors, medical ultrasonic imaging, sensors and actuators, gas ignitors, transducers, capacitors, and ferroelectric thin film memories [1–9]. Among the known piezoelectric ceramics, lead (Pb) based materials, such as lead zirconate titanates ( $\text{PbZr}_{1-x}\text{Ti}_x\text{O}_3$ , PZT), exhibit the superior properties. The PZT ceramics exhibit the higher piezoelectric coefficient ( $d_{33}$ ) > 400 pC/N and a Curie temperature ( $T_c$ )  $\sim 590$  K, which are primarily due to the presence of morphotropic phase boundary (MPB) region between rhombohedral (*R*) and tetragonal (*T*) phases of PZT [1–4]. However, PZT contains more than 60 wt% of Pb, which is toxic in nature. The large amount of toxic Pb-content creates health and environmental hazards [5]. Therefore, for health and environmental protection, the design and development of Pb-free ferroelectric/piezoelectric materials with

properties comparable or better than the well-known PZT materials is highly desired.

Among the existing Pb-free piezoelectric materials, barium titanate ( $\text{BaTiO}_3$  (BT)) and BT-based materials are of great practical interest due to their excellent properties such as relatively high chemical stability and ability to easily sinter while maintaining the chemical stoichiometry [2,5–9]. Recently, extensive efforts were directed to synthesize the modified BT ceramics near the MPB region composition [10,11]. The BT ceramics modified with Sn,  $(1-x)\text{BaTiO}_3\text{-}x\text{BaSnO}_3$  and  $(\text{Ba,Ca})(\text{Ti}_{1-x}\text{Sn}_x)$ , exhibit superior piezoelectric ( $d_{33} \sim 600\text{--}700$  pC/N) properties compared to PZT [12,13]. However, despite the higher  $d_{33}$  values, lower value of  $T_c$  ( $\sim 313$  K) limits their practical applications [12,13]. Nevertheless, Liu and Ren have recently reported that the  $(\text{Ba}_{0.7}\text{Ca}_{0.3})\text{TiO}_3\text{-Ba}(\text{Ti}_{0.8}\text{Zr}_{0.2})\text{O}_3$  (BCT-*x*BZT) system, where the MPB region originates from a critical point of a cubic paraelectric phase (*C*), ferroelectric *R* and *T* phases, exhibits the giant piezoelectric coefficient ( $d_{33}$ )  $\sim 620$  pC/N [14]. However, the presence of an intermediate

\* Corresponding authors.

E-mail addresses: [ydk@physics.unipune.ac.in](mailto:ydk@physics.unipune.ac.in) (Y.D. Kolekar), [rvchintalapalle@utep.edu](mailto:rvchintalapalle@utep.edu) (C.V. Ramana).

<https://doi.org/10.1016/j.ceramint.2018.06.115>

Received 2 April 2018; Received in revised form 17 May 2018; Accepted 13 June 2018

Available online 15 June 2018

0272-8842/ © 2018 Elsevier Ltd and Techna Group S.r.l. All rights reserved.

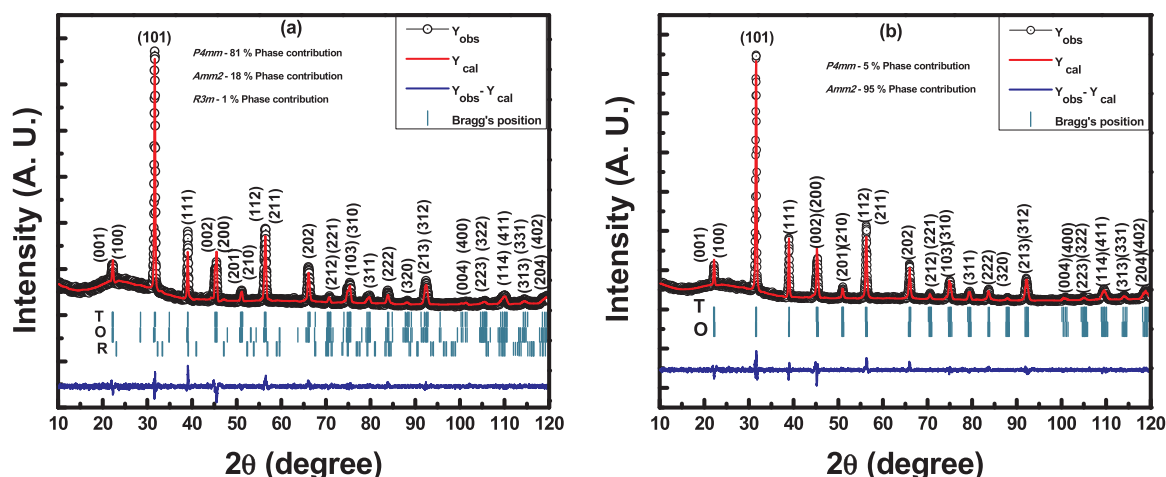


Fig. 1. Room temperature Rietveld fitted XRD patterns for (a) 55BCT30 and (b) 45BCT30.

orthorhombic (O) phase is also noted; this intermediate O symmetry may be related to the large piezoelectric response in the BCT-xBZT system [15–19], which calls upon further fundamental scientific investigation. Furthermore, a fundamental understanding of the structural characteristics and structure-property relationship of the BCT-xBZT system near the MPB region is currently lacking [20,21]. Therefore, in the present work, an attempt has been made to investigate and derive a comprehensive understanding of the structure-property relationship in the BCT-xBZT system, specifically the  $(1-x)\text{Ba}_{0.7}\text{Ca}_{0.3}\text{TiO}_3$ - $x\text{BaTi}_{0.8}\text{Zr}_{0.2}\text{O}_3$  ( $x = 0.45, 0.55$ ; abbreviated as 55BCT30 and 45BCT30) ceramics near MPB region. Combined use of X-ray diffraction (XRD), Rietveld refinement and temperature dependent Raman spectra allowed us to probe the structural characteristics precisely. The results and analyses are presented and discussed to establish a correlation between structural, ferroelectric, piezoelectric and dielectric properties of the 55BCT30 and 45BCT30 ceramics along with a comparison of the data with those reported for Pb-free ceramics.

## 2. Materials and methods

### 2.1. Synthesis

Lead-free  $(1-x)\text{Ba}_{0.7}\text{Ca}_{0.3}\text{TiO}_3$ - $x\text{BaTi}_{0.8}\text{Zr}_{0.2}\text{O}_3$  (where  $x = 0.45, 0.55$ ) ceramics, which are abbreviated as 55BCT30 and 45BCT30, were synthesized by the standard solid state ceramic reaction method. High purity ( $> 99\%$ ) oxides viz.,  $\text{BaCO}_3$ ,  $\text{CaCO}_3$ ,  $\text{TiO}_2$  and  $\text{ZrO}_2$  (Sigma Aldrich) were used in ceramic synthesis. The stoichiometric amounts of precursors were grinded in an ethanol medium and were calcined at  $850^\circ\text{C}$  and  $1050^\circ\text{C}$  for 10 h followed by pre-sintering at  $1250^\circ\text{C}$  for 5 h at ambient atmosphere with intermediate grindings. Then, the powders were grounded again by adding polyvinyl alcohol (PVA) as a binder and pressed into pellets (diameter  $\sim 10$  mm, thickness  $< 1$  mm) using hydraulic press and finally sintered at  $1400^\circ\text{C}$  for 5 h.

### 2.2. Characterization

The X-ray diffraction (XRD) measurements were performed on the ceramics using a Bruker D8 Advance X-ray diffractometer (XRD) ( $\text{Cu } k_\alpha$  having  $\lambda = 1.5406 \text{ \AA}$ ). The scans were made in the  $2\theta = 10$ – $120^\circ$  range with a step size of  $0.02^\circ$ . Rietveld refinements were performed on the XRD data employing Fullprof software. For the Rietveld refinement, shape of Bragg peaks was modified by Pseudo-Voigt function, which is a combination of Gaussian and Lorentzian function. The background of XRD pattern was fitted with the linear interpolation method between a set of background points and refinable heights. During the fitting process, the scale factors, cell parameters, shape parameters, FWHM

parameters, and zero angular shifts were refined. For detailed structural and phase transition analyses, temperature dependent ( $90$ – $450$  K) Raman spectra were obtained using Renishaw Invia Raman spectroscopy system LEICA DM 2500 M having  $532 \text{ nm}$  Ar ion laser excitation source. The morphology of the samples was studied with the help of scanning electron microscope (SEM) (JEOL JSM 6360). For the ferroelectric, piezoelectric and dielectric measurements, pellets were polished and then electroded on both the sides of polished surface using silver paste and heated at  $100^\circ\text{C}$  for overnight to cure the silver paste. The electroded samples were then used for polarization versus electric field (P-E) hysteresis and field-induced strain (S-E) hysteresis loop measurements using a ferroelectric test system (aixAcct systems, GMBH TF ANALYSER 2000 TREK model 610 E) at an applied frequency of  $0.1 \text{ Hz}$ . The dielectric measurements were then performed for all the samples, using HIOKI 3532-50 LCR HiTESTER, in the temperature range of  $150$ – $450 \text{ K}$ . After these measurements, electric poling was performed on all the electroded samples for 30 min each at an applied dc electric field of  $\sim 10 \text{ kV/cm}$ . The piezoelectric charge coefficient ( $d_{33}$ ) was then measured using a YE2730A  $d_{33}$  meter (APC International Ltd.).

## 3. Results and discussion

### 3.1. Crystal structure and phase analysis

The XRD data of the ceramics are shown in Fig. 1. It can be noted that the 55BCT30 and 45BCT30 ceramics exhibit the polycrystalline perovskite crystal structure without any traces of impurity/secondary phase. To understand the crystal structure and phase transformations (if any), the splitting of XRD characteristic peaks observed at  $2\theta \approx 45^\circ, 56^\circ, 66^\circ$  and  $84^\circ$  are considered for further analysis. The detailed view of the characteristic peak splitting at the respective  $2\theta$  values are presented in Fig. 2. It is observed that, for 55BCT30 and 45BCT30, more than one phase coexists. The clear splitting of the peak around  $2\theta \approx 45^\circ$  i.e. (002)/(200) for 55BCT30 indicates the tetragonal (T) phase. However, for 45BCT30, no clear splitting or separated peaks were observed at  $2\theta \approx 45^\circ$  which indicates the decrease in T-phase contribution with increase of Zr content [22,23]. At  $2\theta \approx 56^\circ$ , merged peaks [(112)/(211)] for T and [(113)/(131)/(202)] for O resulted into one asymmetric hump in both the samples [24]. The merged peak at  $2\theta \approx 66^\circ$  for 55BCT30 is more asymmetric compared to 45BCT30. It is easily split into two peaks which indicates that, for 55BCT30, R-phase also exists along with O-phase. Similarly, for  $2\theta \approx 84^\circ$ , characteristic feature of R-phase has been observed for 55BCT30 i.e., splitting of peaks [(204)/(240)] for O and [(222)/(22-2)] for R [15,25]. Rietveld refinement of the XRD data was performed for all the samples. The 55BCT30 sample was refined with T

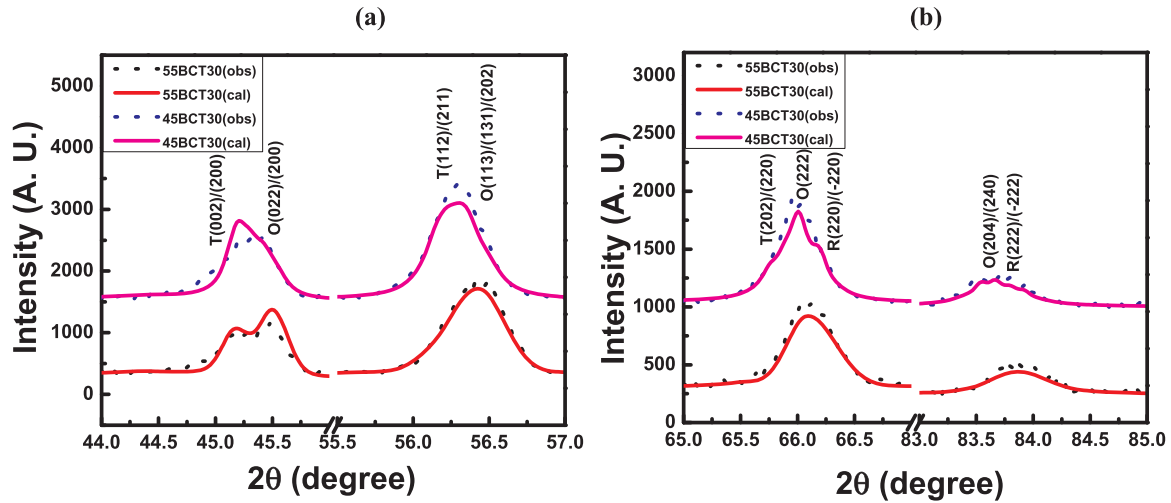


Fig. 2. Enlarged view for splitting of characteristic XRD peaks around (a)  $2\theta \approx (45^\circ \& 56^\circ)$  and (b)  $2\theta \approx (66^\circ \& 84^\circ)$ .

Table 1

Lattice parameters ( $a$ ,  $b$  and  $c$ ), unit cell volume ( $V$ ), % phase contribution, Bragg R-factor,  $R_f$  factor, chi square ( $\chi^2$ ), goodness of fit factor ( $Goff$ ) for 55BCT30 and 45BCT30 ceramics.

Composition		$a$ (Å)	$b$ (Å)	$c$ (Å)	$V$ (Å) <sup>3</sup>	% Phase contribution	Bragg R-factor	$R_f$ factor	$\chi^2$	Goff ( $\frac{R_{wP}}{R_{exp}}$ )
55BCT30	T	3.9860(2)	3.9860(2)	4.0139(2)	63.77	80.61(1.42)	6.05	4.20	1.73	1.32
	O	3.9846(4)	5.6927(13)	5.6573(6)	128.32	18.18(0.74)	6.47	3.09		
	R	5.3742(10)	5.3742(10)	6.9059(11)	172.68	1.21(0.02)	5.56	2.89		
45BCT30	T	3.9969(0)	3.9969(0)	4.0190(0)	64.203	5.19(0.34)	6.05	4.20	1.79	1.34
	O	3.9898(0)	5.6659(0)	5.6760(0)	128.31	94.81(1.66)	4.81	2.61		

Note: T – Tetragonal; O – Orthorhombic; R – Rhombohedral.

( $P4mm$ ), O ( $Amm2$ ) and R ( $R3m$ ) while 45BCT30 sample with T ( $P4mm$ ) and O ( $Amm2$ ). The resulting refined parameters are presented in Table 1. The lower values of Bragg R-factor and  $R_f$  factor of individual phases (T, O and R) indicates the good fitting of data for the respective individual phases. Furthermore, the values of  $\chi^2$  and goodness of fit factor ( $Goff$ ) are also low which indicate that the whole pattern is fitted well and the good agreement between the calculated and observed patterns. It is also observed from Table 1 that, for 55BCT30, major ( $\sim 80\%$ ) contribution comes from T-phase which can be correlated to the well separated XRD peaks (002)/(200) at  $2\theta \approx 45^\circ$ . For 45BCT30, major ( $\sim 94\%$ ) contribution comes from O phase [merged peaks at  $2\theta \approx 66^\circ \& 84^\circ$ ]. Thus, XRD analyses confirm the coexistence of all three (T + O + R) phases for 55BCT30 and two (T + O) phases for 45BCT30.

### 3.2. Chemical bonding

A more detailed account of structural and chemical bonding information was probed using temperature dependent Raman spectroscopic measurements. Fig. 3 shows the temperature dependent Raman spectra of 55BCT30 and 45BCT30 ceramics in the temperature range of 93–450 K. The observed Raman modes as a function of temperature are tabulated in Tables 2 and 3 for 55BCT30 and 45BCT30 ceramics, respectively. The observed Raman modes for the 55BCT30 and 45BCT30 ceramics are similar to that of pure  $BaTiO_3$  and are in good agreement with those reported in literature [24,26]. Along with the modes corresponding to pure  $BaTiO_3$ , an extra feature is observed at  $\sim 132\text{ cm}^{-1}$ . This extra feature, which is present in the Raman spectra in the entire temperature range, corresponds to Zr replacing Ti [27]. It is observed from Fig. 3(a) that, for 55BCT30, the Raman spectra show similar features in the 93–200 K and 250–295 K range. The  $A_1(LO)$  mode at  $\sim 157\text{ cm}^{-1}$  starts becoming weak after 340 K which indicates the

absence of R-phase above 340 K. However, at room temperature (295 K), the characteristic signature of T + O + R phases namely  $A_1(LO) \sim 150\text{ cm}^{-1}$ , sharp interference dip  $\sim 180\text{ cm}^{-1}$ , broad and wide  $E(LO_1 + TO_1)/A_1(TO_2) \sim 230\text{ cm}^{-1}$  and  $A_1(LO)/E(LO) \sim 726\text{ cm}^{-1}$  are present. The simultaneous presence of these modes indicates that all three phases (T + O + R) coexist in these ceramics which is also evident in the XRD analyses. The interference dip at  $\sim 180\text{ cm}^{-1}$ ,  $E(LO + TO)/B_1 \sim 295\text{ cm}^{-1}$  and  $A_1(LO)/E(LO) \sim 726\text{ cm}^{-1}$  starts becoming weak after 360 K and completely disappears at 405 K. This observation indicates the ferroelectric to paraelectric phase transition. Furthermore, in the present case, the O to T phase transition is not detected in the Raman spectra in the temperature range of 93–380 K which may be due to the coexistence of T + O + R phases and their similar Raman spectral features. Also, due to the increase in broadness of the Raman modes with increasing temperature, the characteristic feature of O phase i.e.,  $E(LO_1 + TO_1)/A(LO) \sim 190\text{ cm}^{-1}$  is not noticeable which may be due to its merging with  $A_1(TO_2) \sim 230\text{ cm}^{-1}$ . In the case of 45BCT30 ceramics, the merged  $E(LO_1 + TO_1)$  mode at  $\sim 200\text{ cm}^{-1}$  can be clearly seen from the asymmetric behavior of wide and broad  $A_1(TO_2)$  mode at  $250\text{ cm}^{-1}$  which implies the existence of O phase (Fig. 3b). The sharpness of interference dip at  $\sim 180\text{ cm}^{-1}$  and the intensity of tetragonal characteristic Raman modes, such as  $E(LO + TO)/B_1 \sim 294\text{ cm}^{-1}$  and  $A_1(LO)/E(LO) \sim 720\text{ cm}^{-1}$ , decreases in 45BCT30 compared to 55BCT30. This observation indicates the decrease in T phase contribution for 45BCT30 ceramics which is also evident in XRD analyses. Also, the characteristic feature of T + O phase was completely disappeared at 380 K for 45BCT30 which indicates the ferroelectric to paraelectric phase transition. Furthermore, for both the 55BCT30 and 45BCT30 ceramics, the  $E(TO)/A_1(TO_3) \sim 530\text{ cm}^{-1}$  mode shifts toward lower frequency with increasing temperature. This feature indicates the complete incorporation of  $Zr^{4+}$  at  $Ti^{4+}$  site [22]. Thus, the temperature dependent Raman

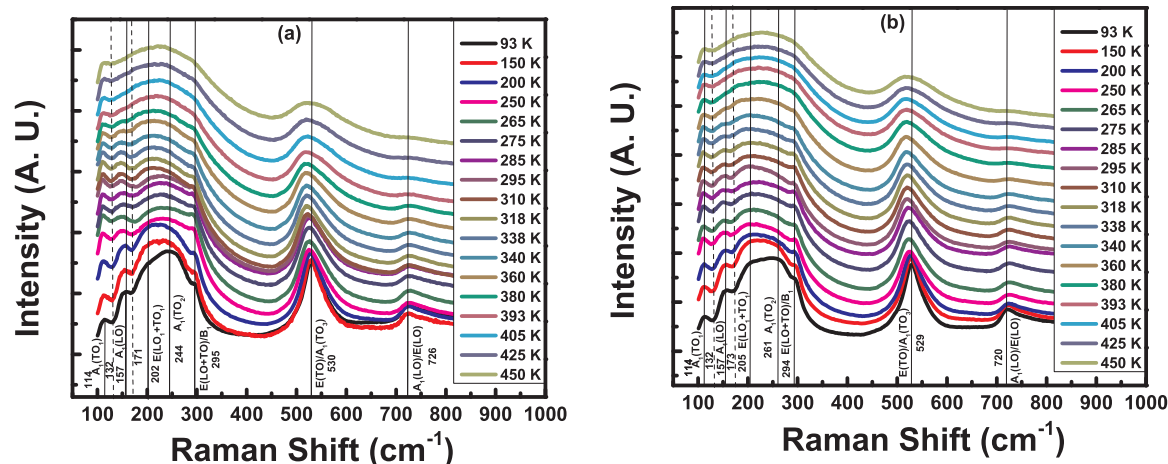


Fig. 3. Temperature dependent Raman spectra for (a) 55BCT30 and (b) 45BCT30.

spectroscopic analyses confirm the coexistence of multiple phases for both the 55BCT30 (T + O + R) and 45BCT30 (T + O) as noted in XRD analyses.

### 3.3. Microstructure

The SEM micrographs and elemental mapping of the samples are presented in Fig. 4. A well connected polyhedral shaped grain with a dense microstructure is evident in these SEM images. The average grain size for the 55BCT30 and 45BCT30 ceramics is in the range of 5–7  $\mu\text{m}$ . Also, the elemental mapping (Fig. 4b,d) data indicates the homogeneous distribution of the constituent elements. Thus, the SEM and elemental mapping analyses confirm the dense, non-porous and homogeneous microstructure of the samples.

### 3.4. Ferroelectric and piezoelectric properties

Fig. 5 presents the typical ferroelectric (P-E) hysteresis loops for 55BCT30 and 45BCT30 Pb-free ceramics, at room temperature, confirming their ferroelectric nature. The ferroelectric parameters, namely maximum polarization ( $P_{\text{max}}$ ), remnant polarization ( $P_r$ ) and coercive field ( $E_c$ ), obtained from P-E hysteresis loops are tabulated in Table 4. These parameters determined from P-E hysteresis loops of 55BCT30 and 45BCT30 ceramics are comparable with those reported in the literature

[14,22,23]. However, compared to 55BCT30, 45BCT30 ceramics exhibit higher values of  $P_{\text{max}}$  and  $P_r$  and lower  $E_c$  values (Fig. 5). Also, the polarization increases by almost 60% while  $E_c$  becomes almost half for the 45BCT30 ceramics compared to 55BCT30 ceramics. The observed high values of  $P_r$  in the present case, may be due to the compositional homogeneity, low defect density, uniform distribution of grain size, and absence of domain wall pinning centers [2]. Lower  $E_c$  values observed in the 45BCT30 ceramics indicate that the ceramics become softer with increase in  $x$  i.e., for  $x = 0.55$ . Thus, for 45BCT30, low electric field is required to align the domains so that it can be used for switching applications. Also, this may be ascribed to the anisotropically flattened free energy profile for polarization rotation around MPB region which causes the lower energy barriers for polarization rotation. Furthermore, these low energy barriers make it easy and assist the polarization rotation and enhanced the piezoelectric properties [24,28].

The variation of polarization current density ( $J$ ) with the applied electric field ( $E$ ) is presented in Fig. 6. The presence of two sharp peaks in opposite direction (Fig. 6) indicate the presence of two stable states with opposite polarity [29] while the maximum current density ( $J_{\text{max}}$ ) is associated with the polarization switching. The observed  $J_{\text{max}}$  values and their corresponding electric fields are summarized in Table 5. It is observed (Table 5) that the 45BCT30 ceramics exhibit higher value of  $J_{\text{max}}$  ( $\sim 52 \times 10^{-5} \text{ A/cm}^2$ ), which is almost twice, at lower electric field, than that of 55BCT30. This may be related to the observed

Table 2

Temperature dependent Raman data for 55BCT30.

Temperature (K)	Raman modes with their positions ( $\text{cm}^{-1}$ )						
	$A_1(\text{TO}_1)$	$A_1(\text{LO}_1)$	$E(\text{LO}_1 + \text{TO}_1)$	$A(\text{TO}_2)$	$E(\text{LO} + \text{TO})/B_1$	$E(\text{TO})/A_1(\text{TO}_3)$	$A_1(\text{LO})/E(\text{LO})$
93	114	157	202	244	295	530	726
150	113	155	merged	227	293	530	726
200	112	157		224	294	529	727
250	111	149		229	292	525	726
265	111	150		230	290	525	727
275	110	151		229	292	526	728
285	110	151		230	291	525	728
295	111	148		228	291	523	727
310	111	148		Broad.....here after	291	522	724
318	110	147			291	523	727
328	110	148			292	521	726
340	111	150			289	520	727
360	110	151			289	522	727
380	110	–			289	521	728
393	112	–			290	519	727
405	113	–			–	522	–
425	114	–			–	522	–
450	114	–			–	525	–



**Table 3**  
Temperature dependent Raman data for 45BCT30.

Temperature (K)	Raman modes with their positions ( $\text{cm}^{-1}$ )						
	$A_1(\text{TO}_1)$	$A_1(\text{LO}_1)$	$E(\text{LO}_1 + \text{TO}_1)$	$A(\text{TO}_2)$	$E(\text{LO} + \text{TO})/\text{B}_1$	$E(\text{TO})/\text{A}_1(\text{TO}_3)$	$A_1(\text{LO})/\text{E}(\text{LO})$
93	114	157	208	250	294	529	720
150	112	157	merged	249	293	527	724
200	112	155		merged	293	528	723
250	111	154			293	525	726
265	111	151			293	524	726
275	111	151			291	524	725
285	111	151			292	521	727
295	110	153			291	520	7226
310	111	152			291	519	724
318	110	153			290	519	726
328	111	152			290	520	723
340	110	152			288	519	725
360	112	Started merging			291	519	726
380	112	–			–	519	–
393	114				–	518	–
405	112				–	518	–
425	114				–	520	–
450	113				–	521	–

increase in  $P_r$  and decrease in  $E_c$  values of 45BCT30 ceramics compared to 55BCT30 [28]. The enhanced values of  $J_{\text{max}}$  for 45BCT30 ceramics can also be attributed to the increase in contribution of O-phase fraction which indicates the susceptibility (tendency) for the polarization switching from (001)T to (011)O, upon application of an electric field [30].

The bipolar S-E hysteresis loops of 55BCT30 and 45BCT30 ceramics are shown in Fig. 7. All the samples exhibit a typical S-E butterfly loop, which confirms their piezoelectric nature. It is observed (Fig. 7) that both the samples exhibit symmetric S-E hysteresis loops which indicate their homogeneity. From S-E hysteresis loop, the converse piezoelectric coefficient ( $d_{33}^*$ ), maximum % strain ( $\%S_{\text{max}}$ ) and their corresponding electric field values are calculated and then averaged out for both the positive and negative electric fields (Table 6). It is observed that the 45BCT30 ceramics exhibit higher values of  $\%S_{\text{max}}$  (at lower field) and  $d_{33}^*$ . The higher values of  $\%S_{\text{max}}$  and  $d_{33}^*$ , observed at lower electric field,

indicates the soft elastic nature of crystal lattice of 45BCT30 ceramics compared to 55BCT30. The origin for this may be due to the presence of MPB region close to this composition as widely reported in the literature [14,28].

The direct piezoelectric coefficient ( $d_{33}$ ) values were measured after poling at room temperature. The data are presented in Table 6. It is observed that 45BCT30 exhibits higher value of  $d_{33}$  compared to 55BCT30 which may be due to the higher  $P_r$  and lower  $E_c$ . This may be also due to the higher O-phase fraction ( $\sim 95\%$ ), which makes it more non-centrosymmetric and enhances the piezoelectric properties of 45BCT30 ceramics compared to 55BCT30 ceramics. Furthermore, it is reported in the literature that along the orthorhombic to tetragonal phase boundary in  $(1-x)\text{Ba}_{0.7}\text{Ca}_{0.3}\text{TiO}_3\text{-xBaTi}_{0.8}\text{Zr}_{0.2}\text{O}_3$  MPB region based composition, giant piezoelectric properties are observed due to the presence of reduced anisotropy energy, high  $P_r/P_{\text{max}}$  ratio and the increased elastic softening which makes the polarization rotation easier

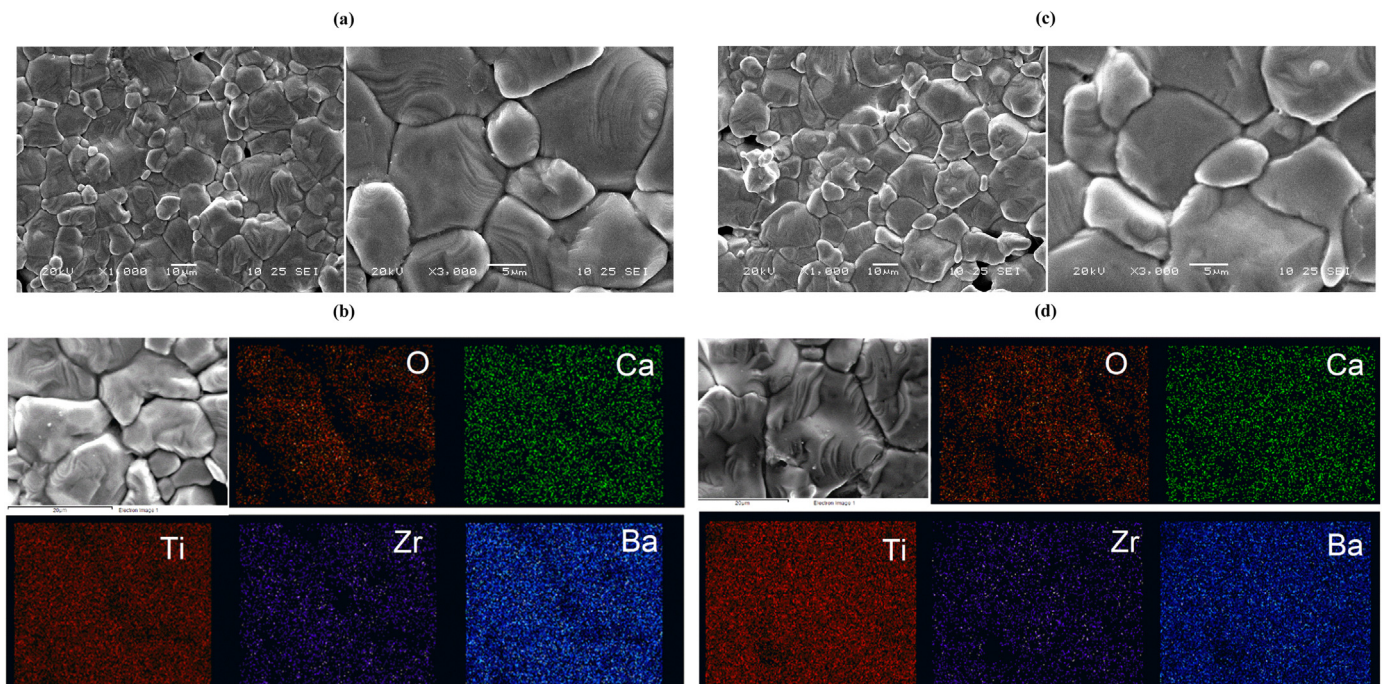


**Fig. 4.** SEM images and elemental mapping of (a) & (b) for 55BCT30 and (c) & (d) for 45BCT30.

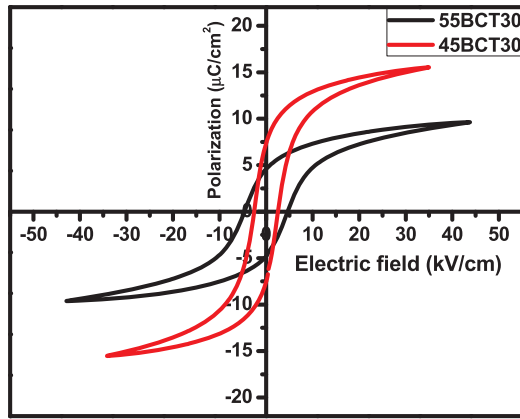


Fig. 5. P-E hysteresis loops for 55BCT30 and 45BCT30.

Table 4

Maximum polarization ( $P_{max}$ ), remnant polarization ( $P_r$ ), squareness ratio ( $P_r/P_{max}$ ) and coercive electric field ( $E_c$ ) values for 55BCT30 and 45BCT30 ceramics.

Composition	$P_{max}$ ( $\mu\text{C}/\text{cm}^2$ )	$P_r$ ( $\mu\text{C}/\text{cm}^2$ )	$\left(\frac{P_r}{P_{max}}\right)$	$E_c$ kV/cm
55BCT30	9.63 (0.15)	4.69 (0.15)	0.48	4.65 (0.21)
45BCT30	15.53 (0.10)	7.35 (0.14)	0.47	2.56 (0.03)

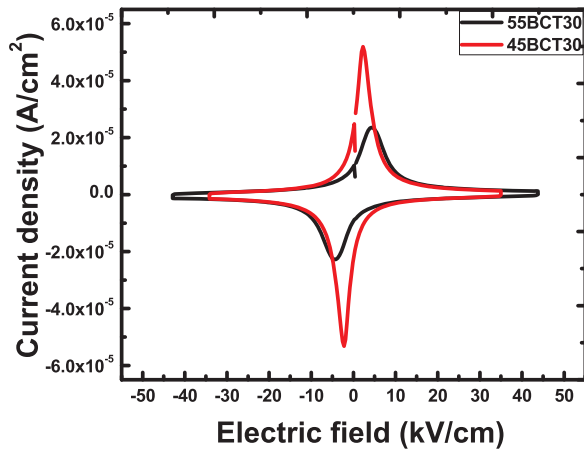


Fig. 6. Variation of current density with applied electric field for 55BCT30 and 45BCT30.

Table 5

Polarization current density ( $J_{max}$ ) values and their corresponding electric field (E) for 55BCT30 and 45BCT30 ceramics.

Composition	Polarization current density $J_{max} \times 10^{-6}$ ( $\text{A}/\text{cm}^2$ )	Electric field (E) kV/cm
55BCT30	23.47 (0.05)    -22.79 (0.39)	4.31 (0)    -4.39 (0)
45BCT30	51.94 (0.09)    -53.20 (0.84)	2.25 (0)    -2.23 (0)

[16,25].

The variation of %strain with polarization is shown in Fig. 8. The electrostrictive coefficient ( $Q_{33}$ ) was calculated using  $Q_{33} = (S_3)/(P_3)^2$ , where,  $Q_{33}$  is the electrostrictive coefficient,  $S_3$  is the induced strain,  $P_3$  is the polarization. The calculated values of  $Q_{33}$  are also tabulated in Table 4. Compared to 55BCT30, 45BCT30 ceramics exhibit lower value of  $Q_{33}$ , which can be correlated to its enhanced piezoelectric properties as observed from  $d_{33}$  and  $d_{33}^*$  values ( $\sim 370$  pC/N and  $\sim 380$  pm/V, respectively). Furthermore, compared to the Pb-based electrostrictive

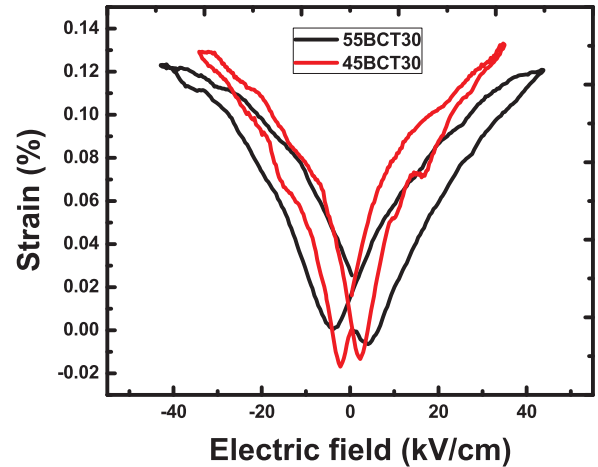


Fig. 7. Bipolar S-E hysteresis loops for 55BCT30 and 45BCT30.

Table 6

Strain (%), electric field at maximum strain ( $E_{max}$ ), converse piezoelectric coefficient ( $d_{33}^*$ ), direct piezoelectric coefficient ( $d_{33}$ ) and electrostrictive coefficient ( $Q_{33}$ ) for 55BCT30 and 45BCT30 ceramics.

Composition	Strain (%)	$E_{max}$ kV/cm	$d_{33}^*$ pm/V	$d_{33}$ pC/N	$Q_{33} \times 10^{-2}$ m <sup>4</sup> /C <sup>2</sup>
55BCT30	0.124 (0.007)	43.37 (0.01)	286	355	13.39 (0.94)
45BCT30	0.131 (0.005)	34.59 (0.01)	379	369	5.84 (0.13)

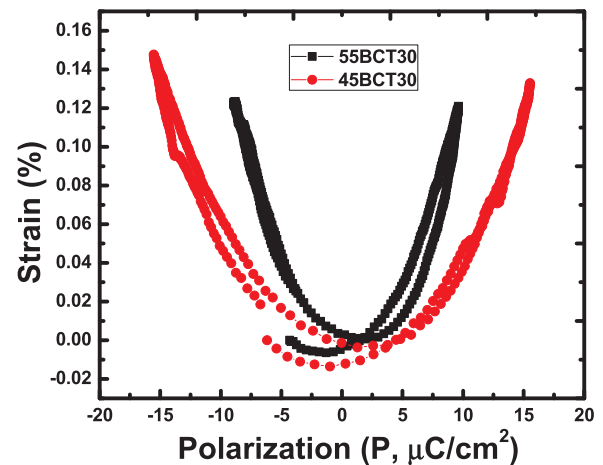


Fig. 8. Strain (%) – Polarization (P) loops for 55BCT30 and 45BCT30.

materials such as  $\text{PbMgNbO}_3\text{-PbTiO}_3$  (PMN-PT,  $Q_{33} = 0.026$  m<sup>4</sup>/C<sup>2</sup>), the  $Q_{33}$  values observed for 55BCT30 and 45BCT30 ceramics are relatively higher [31,32].

### 3.5. Dielectric properties

The variation of dielectric constant ( $\epsilon'$ ) with temperature at different frequencies are shown in Fig. 9. The data shown are in the temperature range of 150–460 K. It is observed (Fig. 9) that, for 55BCT30 and 45BCT30, the transition temperature does not change with frequency. The observed values of transition temperature and their corresponding dielectric maxima are tabulated in Table 7. In the case of 55BCT30 ceramics, the ferroelectric phase transition temperature (i.e., R/O to T phase) was found to be near room temperature (303 K) while ferroelectric to paraelectric (i.e., T to C) phase is  $\sim 388$  K. This indicates

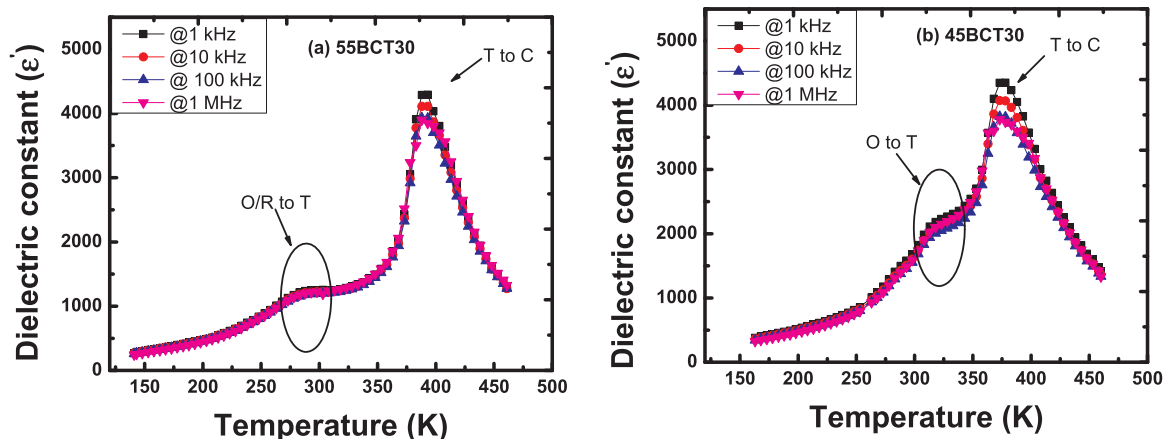


Fig. 9. Variation of dielectric constant as a function of temperature at different frequencies for (a) 55BCT30 and (b) 45BCT30.

Table 7

Transition temperature, Dielectric constant ( $\epsilon'$ ) at transition temperatures for different frequencies.

Composition	Transition Temperature K	$\epsilon'$ at Transition Temperature			
		1 kHz	10 kHz	100 kHz	1 MHz
55BCT30	303 (R/O -T)	1254	1227	1200	1190
	388 (T <sub>c</sub> )	4288	4110	3934	3900
45BCT30	298–323 (O-T)	~ 2000	~ 2000	~ 2000	~ 2000
	373 (T <sub>c</sub> )	4350	4072	3825	3780

Note: R/O-T and T-C represents rhombohedral/orthorhombic to tetragonal phase transition and tetragonal to cubic phase transition (T<sub>c</sub>) temperatures, respectively.

that, for 55BCT30, all the ferroelectric phases i.e., R, O and T, coexist. These results are in excellent agreement with the conclusions derived from XRD and temperature dependent Raman spectroscopic analyses. However, on the other hand, for 45BCT30, the ferroelectric phase transition temperature (i.e., O to T) becomes broad in the temperature range of 298–325 K and shifts to higher temperature (compared to 55BCT30) while ferroelectric to paraelectric (i.e., T to C) phase is at ~ 373 K. Again, these results are corroborated with the results obtained from XRD and temperature dependent Raman scattering data analyses. The shift of O to T phase transition to higher temperature is due to the increase of BZT content in 45BCT30; this observation is in agreement with the literature [27]. Also, the values of dielectric constant of the 55BCT30 and 45BCT30 ceramics are higher indicating their potential applicability in capacitor devices.

#### 4. Conclusions

In summary, the 55BCT30 and 45BCT30 ceramics close to MPB region were successfully synthesized by the conventional solid state ceramic reaction method. The XRD patterns along with the Rietveld refinement indicate the coexistence of R + O + T and O + T phases for 55BCT30 and 45BCT30, respectively, which was further confirmed by the temperature dependent Raman spectroscopic analyses. The dense and non-porous microstructure along with a homogeneous chemical composition was evident in all the ceramics. The presence of typical P-E and S-E hysteresis loops for the 55BCT30 and 45BCT30 ceramics confirm their ferroelectric and piezoelectric nature. The J-E curves demonstrate the presence two stable states with opposite polarity. Higher values of direct piezoelectric coefficient ( $d_{33} > 360$  pC/N) in these ceramics may be due to the existence of low energy barrier around MPB region and polymorphic nature of synthesized ceramics i.e., the coexistence of multiple phases. The 55BCT30 ceramics exhibit higher value of electrostrictive coefficient ( $Q_{33} \sim 0.1339$  m<sup>4</sup>/C<sup>2</sup>) compared to

conventional Pb-based electrostrictive materials. Temperature dependent dielectric measurements also indicate the phase coexistence of 55BCT30 and 45BCT30 near room temperature (consistent with XRD and Raman spectra analyses) and exhibiting Curie temperature in the range from 370 K to 390 K. The 45BCT30 exhibits enhanced piezoelectric and ferroelectric properties due to the existence of T-O phase boundary where polarization rotation can take place easily. Thus, the observed properties show that the 55BCT30 and 45BCT30 ceramics are suitable to serve as Pb-free ferroelectric and piezoelectric materials.

#### Acknowledgements

Bhavna C Keswani is thankful to University Grants Commission (UGC) for providing research fellowship under BSR scheme. Authors are thankful to Prof. Arturo Bronson for his input, critically reading the manuscript, helpful discussions and corrections made. Authors are thankful to the Department of Science and Technology, New Delhi for providing financial assistance (Ref. SR/FTP/PS-040/2010) to carry out the research work. Authors are also thankful to Dr. R. C. Kambale for his support during the experimental measurements. CVR acknowledges with pleasure the support from NSF-PREM grant #DMR-1827745.

#### References

- [1] K. Uchino, *Ferroelectric Devices*, Taylor & Francis Group, New York.
- [2] G.H. Haertling, *Ferroelectric ceramics: history and technology*, *J. Am. Ceram. Soc.* 82 (1999) 797–818.
- [3] C.A. Randall, N. Kim, J. Kucera, W. Caoand, T.R. Shrout, *Intrinsic and extrinsic size effects in fine - grained morphotropic -phase -boundary lead zirconate titanate ceramics*, *J. Am. Ceram. Soc.* 81 (1998) 677–688.
- [4] A.J. Bell, *Factors influencing the piezoelectric behaviour of PZT and other "morphotropic phase boundary" ferroelectrics*, *J. Mater. Sci.* 41 (2006) 13.
- [5] P.K. Panda, *Review: environmental friendly lead-free piezoelectric materials*, *J. Mater. Sci.* 44 (2009) 5049–5062.
- [6] Z. Yu, C. Ang, R. Guo, A.S. Bhalla, *Piezoelectric and strain properties of Ba (Ti<sub>1-x</sub>Zr<sub>x</sub>)O<sub>3</sub> ceramics*, *J. Appl. Phys.* 92 (2002) 1489–1493.
- [7] W. Bai, D. Chen, P. Zheng, J. Zhang, B. Shen, J. Zhai, Z. Ji, *Low electric field-driven giant strain response in < 001 > textured BNT-based lead-free piezoelectric materials*, *J. Mater. Sci.* 52 (2017) 3169–3178.
- [8] K.H. Lam, M.S. Guo, D.M. Lin, K.W. Kwok, H.L.W. Chan, *Lead-free piezoelectric BNKLT 1–3 composites*, *J. Mater. Sci.* 43 (2008) 1677–1680.
- [9] C. Zhou, X. Liu, *Dielectric and piezoelectric properties of bismuth-containing complex perovskite solid solution of Bi<sub>1/2</sub>Na<sub>1/2</sub>TiO<sub>3</sub>-Bi(Mg<sub>2/3</sub>Nb<sub>1/3</sub>)O<sub>3</sub>*, *J. Mater. Sci.* 43 (2008) 1016–1019.
- [10] A.M. Sanz, C. Berger, M.R. Dolgos, *Understanding the structure-property relationships of the ferroelectric to relaxor transition of the (1-x)BaTiO<sub>3</sub>-(x)BiInO<sub>3</sub> lead-free piezoelectricsystem*, *J. Mater. Sci.* 52 (2017) 5309–5323.
- [11] C.W. Ahn, C.H. Choi, H.Y. Park, S. Nahm, S. Priya, *Dielectric and piezoelectric properties of (1-x)(Na<sub>0.5</sub>K<sub>0.5</sub>)NbO<sub>3</sub>-xBaTiO<sub>3</sub> ceramics*, *J. Mater. Sci.* 43 (2008) 6784–6797.
- [12] J. Gao, D. Xue, W. Liu, C. Zhou, X. Ren, *Recent progress on BaTiO<sub>3</sub>-based piezoelectric ceramics for actuator applications*, *Actuators* 6 (2017) 24.
- [13] L.F. Zhu, B.P. Zhang, X.K. Zhao, L. Zhao, F.Z. Yao, X. Han, P.F. Zhou, J.F. Li, *Phase transition and high piezoelectricity in (Ba,Ca)(Ti<sub>1-x</sub>Sn<sub>x</sub>)O<sub>3</sub> lead-free ceramics*,

- Appl. Phys. Lett. 103 (2013) 72905.
- [14] W. Liu, X. Ren, Large piezoelectric effect in Pb-free ceramics, *Phys. Rev. Lett.* 103 (2009) 257602.
- [15] K. Brajesh, M. Abebe, R. Ranjan, Structural transformations in morphotropic-phase-boundary composition of the lead-free piezoelectric system  $\text{Ba}(\text{Ti}_{0.8}\text{Zr}_{0.2})\text{O}_3$ - $(\text{Ba}_{0.7}\text{Ca}_{0.3})\text{TiO}_3$ , *Phys. Rev. B* 94 (2016) 1–7.
- [16] M. Acosta, N. Khakpash, T. Someya, N. Novak, W. Jo, H. Nagata, G.A. Rossetti, J. Rodel, Origin of the large piezoelectric activity in  $(1-x)\text{Ba}(\text{Zr}_{0.2}\text{Ti}_{0.8})\text{O}_3$ - $x(\text{Ba}_{0.7}\text{Ca}_{0.3})\text{TiO}_3$  ceramics, *Phys. Rev. B - Condens. Matter Mater. Phys.* 91 (2015) 1–11.
- [17] D.S. Keeble, F. Benabdallah, P.A. Thomas, M. Maglione, J. Kreisel, Revised structural phase diagram of  $(\text{Ba}_{0.7}\text{Ca}_{0.3}\text{TiO}_3)$ - $(\text{BaZr}_{0.2}\text{Ti}_{0.8}\text{O}_3)$ , *Appl. Phys. Lett.* 102 (2013) 1–6.
- [18] J. Gao, D. Xue, Y. Wang, D. Wang, L. Zhang, H. Wu, S. GUO, H. Bao, C. Zhou, W. Liu, S. Hou, G. Xiao, X. Ren, Microstructure basis for strong piezoelectricity in Pb-free  $\text{Ba}(\text{Zr}_{0.2}\text{Ti}_{0.8})\text{O}_3$ - $(\text{Ba}_{0.7}\text{Ca}_{0.3})\text{TiO}_3$  ceramics, *Appl. Phys. Lett.* 99 (2011) 2013–2016.
- [19] Y. Tian, X. Chao, L. Jin, L. Wei, P. Liang, Z. Yang, Polymorphic structure evolution and large piezoelectric response of lead-free  $(\text{Ba,Ca})(\text{Zr,Ti})\text{O}_3$  ceramics, *Appl. Phys. Lett.* 104 (2014) 10–15.
- [20] V.S. Puli, D.K. Pradhan, D.B. Chirsey, M. Tomozawa, G.L. Sharma, J.F. Scott, R.S. Katiyar, Structure, dielectric, ferroelectric, and energy density properties of  $(1-x)\text{BZT}-x\text{BCT}$  ceramic capacitors for energy storage applications, *J. Mater. Sci.* 48 (2013) 2151–2157.
- [21] M. Jiang, Q. Lin, D. Lin, Q. Zheng, X. Fan, X. Wu, H. Sun, Y. Wan, L. Wu, Effects of  $\text{MnO}_2$  and sintering temperature on microstructure, ferroelectric, and piezoelectric properties of  $\text{Ba}_{0.85}\text{Ca}_{0.15}\text{Ti}_{0.90}\text{Zr}_{0.10}\text{O}_3$  lead-free ceramics, *J. Mater. Sci.* 48 (2013) 1035–1041.
- [22] V.S. Puli Sreenivas, D.K. Pradhan, W. Perez, R.S. Katiyar, Structure, dielectric tunability, thermal stability and diffuse phase transition behavior of lead free BZT–BCT ceramic capacitors, *J. Phys. Chem. Solids* 74 (2013) 466–475.
- [23] A. Srinivas, R.V. Krishnaiah, V.L. Niranjani, S.V. Kamat, T. Karthik, S. Asthana, Ferroelectric, piezoelectric and mechanical properties in lead free  $(0.5)\text{Ba}(\text{Zr}_{0.2}\text{Ti}_{0.8})\text{O}_3$ - $(0.5)(\text{Ba}_{0.7}\text{Ca}_{0.3})\text{TiO}_3$  electroceramics, *Ceram. Int.* 41 (2015) 1980–1985.
- [24] L.F. Zhu, B.P. Zhang, L. Zhao, J.F. Li, High piezoelectricity of  $\text{BaTiO}_3$ - $\text{CaTiO}_3$ - $\text{BaSnO}_3$  lead-free ceramics, *J. Mater. Chem. C* 2 (2014) 4764–4771.
- [25] Z. Le, Z. Ming, W. Liang, Z. Chao, Z. Zhen, Y. Yonggang, Z. Lixue, X. Dezhen, L. Xiaojie, R. Xiaobing, Phase transitions and the piezoelectricity around morphotropic phase boundary in  $\text{Ba}(\text{Zr}_{0.2}\text{Ti}_{0.8})\text{O}_3$ - $x(\text{Ba}_{0.7}\text{Ca}_{0.3})\text{TiO}_3$  lead-free solid solution, *Appl. Phys. Lett.* 105 (2014) 162908.
- [26] C.H. Perry, D.B. Hall, Temperature dependence of the Raman spectrum of  $\text{BaTiO}_3$ , *Phys. Rev. Lett.* 15 (1965) 700–702.
- [27] P.S. Dobal, A. Dixit, R.S. Katiyar, Z. Yu, R. Guo, Micro-Raman scattering and dielectric investigations of phase transition behavior in the  $\text{BaTiO}_3$ - $\text{BaZrO}_3$  system, *J. Appl. Phys.* 89 (2001) 8085–8091.
- [28] J.P. Praveen, K. Kumar, A.R. James, T. Karthik, S. Asthana, D. Das, Large piezoelectric strain observed in sol-gel derived BZT-BCT ceramics, *Curr. Appl. Phys.* 14 (2014) 396–402.
- [29] W.Q. Liao, Y. Zhang, C.L. Hu, J.G. Mao, H.Y. ye, P.F. Li, S.D. Huang, R.G. Xiong, A lead-halide perovskite molecular ferroelectric semiconductor, *Nat. Commun.* 6 (2015) 7338.
- [30] K. Brajesh, K. Tanwar, M. Abebe, R. Ranjan, Relaxor ferroelectricity and electric-field-driven structural transformation in the giant lead-free piezoelectric  $(\text{Ba,Ca})(\text{Ti,Zr})\text{O}_3$ , *Phys. Rev. B - Condens. Matter Mater. Phys.* 92 (2015) 1–8.
- [31] F. Li, L. Jin, Z. Xu, S. Zhang, Electrostrictive effect in ferroelectrics: an alternative approach to improve piezoelectricity, *Appl. Phys. Rev.* 1 (2014) 1.
- [32] K. Uchino, S. Nomura, L.E. Cross, R.E. Newnham, S.J. Jang, Review: electrostrictive effect in perovskites and its transducer applications, *J. Mater. Sci.* 16 (1981) 569–578.